Association of platinum-group elements with chromitite within the Merensky reef, Western Limb, Bushveld Complex: Results of a high resolution mineralogical and geochemical study

Justine Magson[*], Marian Tredoux, Frederick Roelofse

Department of Geology, University of the Free State, P.O. Box 339, Bloemfontein 9300, South Africa

ABSTRACT

We present the results of a high-resolution mineralogical and geochemical study conducted across three intersections of Merensky reef at Impala Platinum Mines on the Western Limb of the Bushveld Complex. We studied two intersections of non-pegmatoidal Merensky reef and one intersection of pegmatoidal Merensky reef in an attempt to reconstruct the petrogenesis of this economically important ore horizon and in order to establish the relationship between non-pegmatoidal and pegmatoidal reef intersections. Our results indicate a much stronger correlation between PGE and Cr than between PGE and S (or Cu as a proxy for sulfides), which favours a model in which chromite and associated PGEs were introduced from a deeper staging chamber to result in the formation of the chromitite layers of the Merensky reef. The geochemistry of chromite in the Merensky reef is suggestive of the fact that the bottom chromitite layer of the pegmatoidal reef is a lateral correlate of the chromitite of the non-pegmatoidal reef, in which only a single chromitite layer occurs. We propose that the Merensky reef at Impala Platinum Mines is a product of the introduction of chromite-laden basal flows into the Bushveld Complex magma chamber and that the relationship between pegmatoidal and non-pegmatoidal reef intersections is related to non-deposition, rather than erosion, as was shown to be the case at other localities within the Western Limb.

© 2018 Elsevier Ltd. All rights reserved.

1. Introduction

The Bushveld Complex lies within the north-eastern portion of South Africa (Fig. 1) and occurs near the middle of the Kaapvaal Craton (Cawthorn et al., 2002b; Clarke et al., 2009). It is the world's largest layered mafic intrusion and is part of the Paleo-proterozoic Bushveld Igneous Province (Walraven et al., 1990), and is renowned for its deposits of chromium and platinum-group elements (PGE) occurring in the Rustenburg Layered Suite of the Complex (Cawthorn, 2010b, 2010a). The Bushveld Complex was emplaced at 2055.91 Ma. (Zeh et al., 2015) concordant in the Western limb and disconcordant in the Eastern and Northern limbs in an intraplate setting (Clarke et al., 2009 and Walraven et al., 1990). Although the consensus opinion in the 1960s–1980s was that the Complex cooled very slowly (see Wager and Brown, 1968), Cawthorn (1999) made a good case that this model is not valid: he suggested that the magmas injected into the

Bushveld Complex were emplaced within 75 000 years and that crystallization took about 200 000 years.

The complex occurs in five limbs, *viz.* the Eastern limb, the Western limb, the Far Western limb, the Northern limb and the South-eastern or Bethal limb, (Cawthorn et al., 2002b), of which four outcrop (the Bethal limb is overlain by younger sediments) (Fig. 1). The Western limb, where the work reported on here was based, extends from west of Pretoria to near Thabazimbi and was emplaced at the level of the Magaliesberg Quartzite (Eales and Cawthorn, 1996) of the Transvaal Supergroup.

The Bushveld Complex can be divided into three subdivisions according to SACS (1980): (1) the mafic to ultramafic rocks of the Rustenburg Layered Suite (RLS); (2) the Lebowa Granite Suite; and (3) the Rashoop Granophyre Suite. The Rooiberg Group of felsic and minor basic volcanic rocks are more closely related to the Bushveld event than to the Transvaal Supergroup and should be included with the subdivisions of the Bushveld Complex (Cawthorn et al., 2006) (Fig. 1), although this is currently not the case. The mafic to ultramafic layered succession of the Bushveld Complex, the RLS, contains 75% and 50% of the world's platinum and palladium resources respectively (Barnes and Maier, 2002). The Bushveld
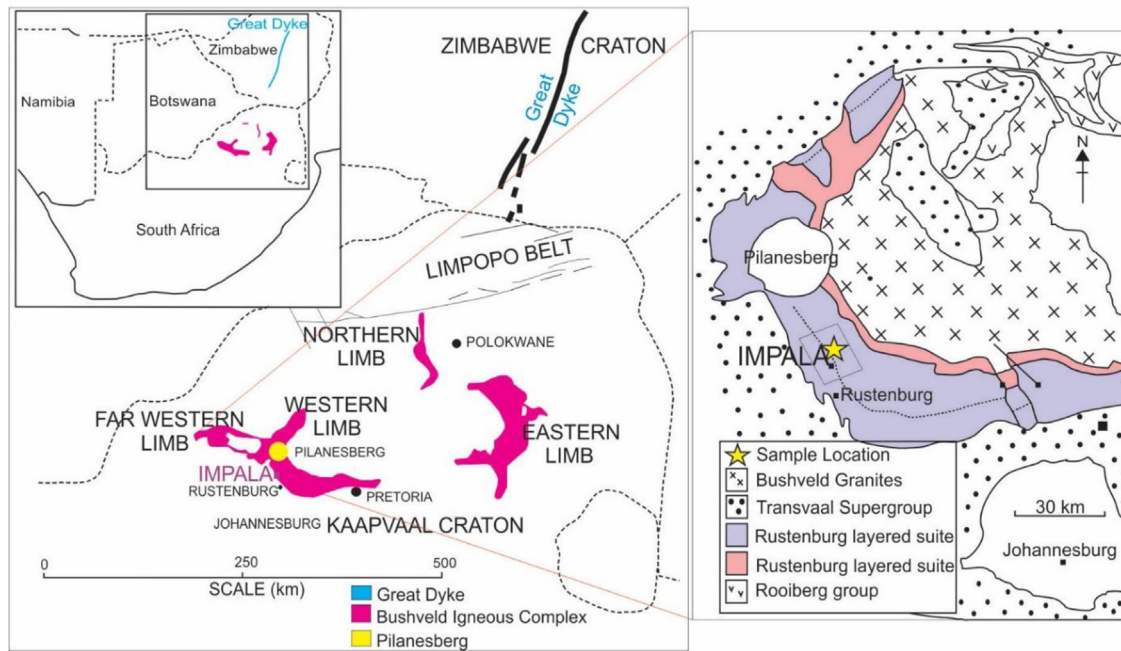
Fig. 1. a) Simplified geological plan, showing the position of the Rustenburg Layered Suite of the Bushveld Complex within South Africa. The location of Impala Platinum Mines in the western Bushveld Complex is also indicated. (Map modified after Scoon and Mitchell, 2009 and Cawthorn et al., 2002a). b) Geology of the Western limb of the Bushveld Complex. The stippled line indicates the outcrop of the Merensky reef. (Map modified after Barnes and Maier, 2002; Maier et al., 2013).

Complex has an areal extent of more than 65 000 km^2 and extends 450 km east-west and 350 km north-south, with the RLS having a thickness of 5–10 km (Eales and Cawthorn, 1996; Cawthorn and Boerst, 2006; Walraven et al., 1990). The RLS is informally subdivided into five different zones by SACS (1980): the Marginal Zone (that forms the base), which is overlain in sequence by the Lower Zone, the Critical Zone, the Main Zone and the Upper Zone, as shown in Fig. 2.

Occurring within the Critical Zone is the world's largest Pt bearing ore bodies: the UG2 and Merensky reefs. The Critical zone can be subdivided into a Lower and Upper Critical Zone, with the transition to the Upper Critical Zone being defined by the introduction of cumulus plagioclase. This transition occurs between the MG2 and MG3 chromitite layers. The Critical Zone displays well-defined layering (see Fig. 2) (Cawthorn et al., 2006). The Upper Critical Zone can further be divided into so-called cyclic units with the following generalised succession in each: basal chromitite – pyroxenite – gabbro – anorthosite (Cawthorn et al., 2006). The MG2 chromitite layer, with its overlying pyroxenite layer is part of the lowest cyclic unit and should therefore be considered as part of the Upper Critical Zone.

The Merensky cyclic unit forms the sixth and penultimate cyclic unit in the Upper Critical zone, and is fairly consistent in thickness (9–10 m) across the Rustenburg section (Viljoen and Hieber, 1986). The Merensky reef and UG2 chromitite have great lateral continuity but in detail can be quite variable (Cawthorn, 2005). The way these reefs formed and became so enriched in PGE is still under investigation and remains poorly understood (Barnes and Maier, 2002). Several models have been proposed over the years to account for the enrichment of PGEs in the Merensky Reef, with the more commonly cited being: (1) sulfide droplets collected PGE and settled to form a layer of PGE-rich minerals (Campbell et al., 1983); (2) the silicate liquid is pre-concentrated with clusters of PGE ions, these are then incorporated into sulfide droplets to crystallize from the magma directly as platinum group minerals (Tredoux et al., 1995; Cawthorn, 1999); (3) a rising intercumulus liquid causes
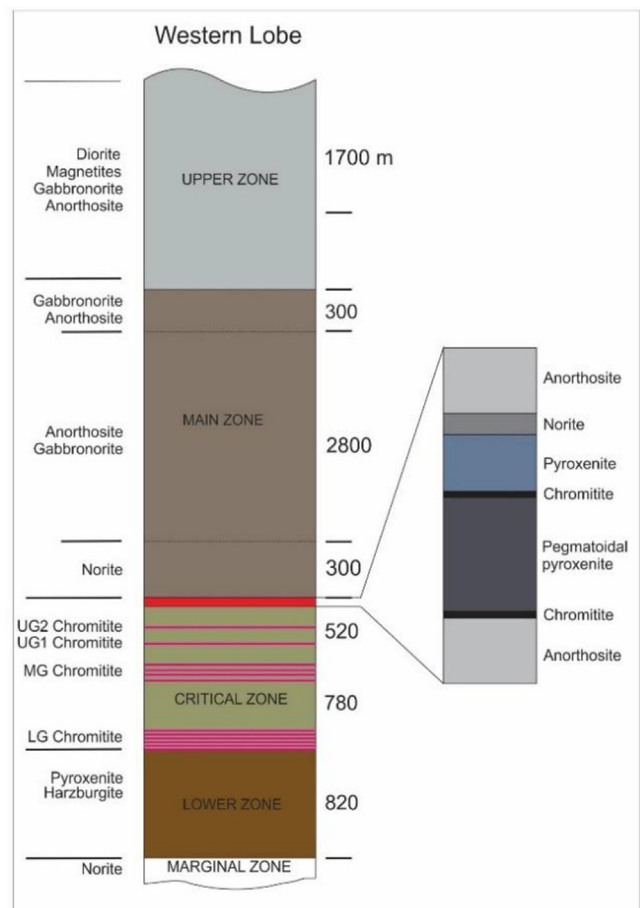
Fig. 2. Idealised section of the layered sequence of the Rustenburg Layered Suite (after Scoon and Mitchell, 2009; Clarke et al., 2009 and Cawthorn and Boerst, 2006); the enlargement shows the Merensky cyclic unit.

the silicate-incompatible PGE to be collected from the cumulate pile and precipitated at the magma-crystal pile interface during compaction and cementation (Willmore et al., 2000; Boudreau and Meurer, 1999); (4) the Complex underwent central subsidence resulting in slumping of unconsolidated cumulates toward the center of the complex. This was accompanied by hydrodynamic redistribution of minerals in slurries to form PGE-bearing sulphide and chromite enriched layers (Maier et al., 2013); (5) the Merensky reef formed from basally emplaced layers of magma, within which crystallization and collection of PGE took place *in situ* (Latypov et al., 2016).

This study presents petrographic, mineralogical and geochemical data on samples from non-potholed pegmatoidal and non-pegmatoidal Merensky reef (see below) from the Impala Platinum Mine (IPM). The results permitted the correlation of the Merensky chromitite layers laterally, to determine which of the two facies in the pegmatoidal reef the single chromitite layer of the non-pegmatoidal reef most closely resembles. It also allowed for the determination of whether the PGE are associated more closely with chromium or sulfur, which has important implications for ore formation models and ore beneficiation protocols.

1.1. The Merensky unit

1.1.1. General features: Merensky reef

The Merensky reef can be traced for a total strike extent of over 280 km, 140 km in both the Western and Eastern limbs. The average dip of the Merensky reef ranges from 9° to 27° towards the center of the Bushveld Complex, but in the northern portion of the Eastern limb, dips as high as 65° have been recorded (Cawthorn et al., 2002a). The term "reef" is a mining term referring to a layer that is enriched in PGE, with a width of about 80 cm (Cawthorn et al., 2002a). PGE concentrations in the Merensky reef can vary significantly and the highest grades are usually associated with chromitite layers. There is significant facies variation in the Merensky unit, mainly associated with different footwall layers. Merensky reef terminology used at IPM and explained by Leeb-Du Toit (1986) are: "A" reef, "B" reef and "C" reef.

1.1.2. The Merensky reef at IPM

The Merensky reef is exploited on the south-western part of the Western limb by IPM (Fig. 1b). IPM defines the Merensky reef as follows: it starts about 30 cm below the lower chromitite (in anorthosite or norite) and it extends upwards to end about 70 cm above the top chromitite (in pyroxenite). The general strike of the Merensky reef is north-north-west to south-south-east, with an average dip of about 9.5° towards the east. Reef outcrop is towards the western boundary of the lease area and at the eastern boundary the reef is more than 2000 m below the surface.

The vertical distribution of PGE in the Merensky reef is variable but to a certain extent a pattern can be established, because the vertical distribution of PGE is also influenced by whether there are two or one chromitite layers. In the case of two chromitite layers, with a significant (>0.5 m) separation between them, the mineralization tends to concentrate higher in the succession, towards the upper chromitite layer to form "top loaded" ores (Cawthorn, 2010a; Davey, 1992). The Merensky reef therefore can be subdivided into either pegmatoidal reef or non-pegmatoidal reef (called pyroxenite reef). In the former case two chromitite stringers are separated by a coarse crystalline mafic "pegmatoidal" layer that can vary in thickness. In the latter case the chromitite layer rests on a footwall of anorthosite and above the chromitite layer is a feldspathic pyroxenite layer (the hangingwall).

2. Methods

The samples investigated originate from three non-potholed drill cores, collected from IPM. Drill core NP (non-pegmatoidal reef) was collected from shaft 14, borehole SD14/90; drill core N (non-pegmatoidal reef) ± 2 km east of shaft 14, borehole BH6259 and drill core P (pegmatoidal reef) from shaft 20, borehole 20/0252. Borehole 20/0252 and SD14/90 were drilled underground and borehole BH6259 is a surface hole (Fig. 3).

In all three cases, samples were taken from the economically mineralized part of the reef. The mining width generally encompasses material from 70 cm above the chromitite stringer to 30 cm below the chromitite stringer for the non-pegmatoidal Merensky reef and 70 cm above the top chromitite stringer to 30 cm below the bottom chromitite stringer for the pegmatoidal Merensky reef. For this project we concentrated on 50 cm above and below the chromitite stringer in the case of the non-pegmatoidal Merensky reef and in the case of the pegmatoidal Merensky reef 10 cm above the top chromitite stringer and 20 cm below the lower chromitite stringer.

The following reef lithologies were observed in the drill core:

- Drill cores SD14/90 and BH6259 (non-pegmatoidal reef): feldspathic pyroxenite, chromitite and anorthosite (Fig. 3a and b).
- Drill core 20/0252 (pegmatoidal reef): feldspathic pyroxenite, chromitite, anorthosite and pegmatoidal pyroxenite (Fig. 3c).

Each core section was cut using a thin diamond studded blade into 2 cm intervals parallel to the chromitite stringer. To ensure an even distribution of sample data along the length of the core, a sample was selected every 6 cm for PGE analysis. However, sampling was concentrated around the chromitite layers (believed to be the more economically mineralized areas) and every 2 cm, for about 6 cm was analyzed (Fig. 3). The selected pieces were then prepared for analysis. Standard thin sections were made for optical and electron microscopy and the rest of the material was finely crushed and aliquots prepared for major and trace element determinations, and for PGE analysis.

2.1. Petrography

Forty-six polished thin sections were prepared, and subjected to optical petrographic examination using transmitted and reflected light. Modal mineralogy was determined by point counting 1000 points per thin section using a mechanical stage. Minerals observed microscopically but not encountered during point counting were assigned concentrations of less than 0.5% by volume. In this project the international standard nomenclature (IUGS) was used to name and classify the different lithologies, with the following additions: The term "feldspathic pyroxenite" is used when no pegmatoidal textures are present and the crystal size is < 20 mm and "pegmatoidal reef" is used when the crystal size exceeds 20 mm.

2.2. Mineral chemistry

The major element composition of minerals in carbon-coated polished thin sections were determined by wavelength-dispersive X-ray spectrometry using a Jeol JXA-8230 Superprobe. Quantitative analyses on plagioclase, pyroxene, chromite, mica and sulfides were performed. At least two spots on 5 separate crystals per thin section were analyzed. The En number was used to denote $100 \times$ cationic ratio of $Mg / (Mg + Fe^{2+} + Ca)$ in pyroxene, the An number to denote $100 \times$ cationic ratio of $Ca/(Ca + Na + K)$ in plagioclase and Mg# to denote the cationic ratio of $Mg/(Mg + Fe^{2+})$.
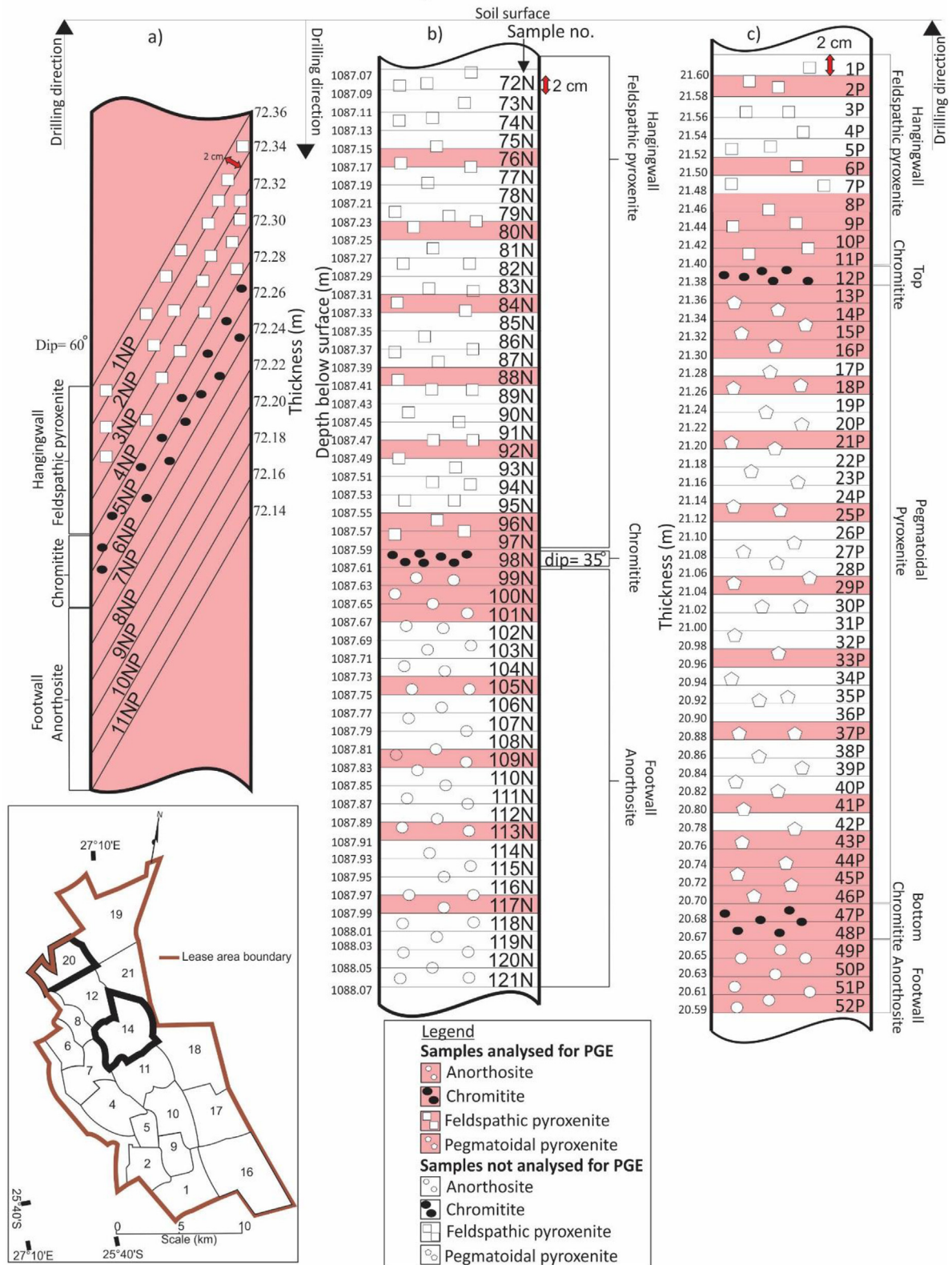
Fig. 3. (a & b) Core log of borehole SD14/90 and BH6259 (respectively) non-pegmatoidal Merensky reef and (c) Core log of borehole 20/0252 pegmatoidal Merensky reef, indicating the different lithologies, drilling direction, samples analyzed, depth of the core section and map of the lease area of IPM with the various shafts.

2.3. Whole-rock geochemistry

2.3.1. Major and trace elements

A portion of every 2 cm core piece was initially reduced in a plastic bag with a hammer and then further reduced to a powder in an agate ring mill. Following crushing, 1 g of each sample was weighed and then heated in a muffle furnace at 900 °C to determine the loss on ignition (LOI). Calibrations were preformed using solutions of the certified reference materials and a blank. 1 ppm Rh spike was used as an internal standard and to correct for instrumental drift over the course of the run. After every sixth sample the standard solution was also repeated for analysis to see if any instrumental drift occurred. The major and trace elements, were determined using the Thermoelemental X series (X7) ICP-MS, equipped with a Meinhard nebulizer and an impact bead spray chamber. For more information about the technique the reader is referred to McDonald and Viljoen (2006) and McDonald and Holwell (2011), which also reports on the accuracy of major elements.

2.3.2. Ultratrace elements (PGE)

Following crushing, samples were prepared for PGE analysis by nickel sulfide fire assay pre-concentration and tellurium co-precipitation as described in McDonald and Viljoen (2006) and Huber et al. (2001). International certified reference materials (WMG-1 and WPR-1) and blanks were prepared in the same manner, but omitting the sample material. The PGE were also determined using the Thermoelemental X series (X7) ICP-MS, equipped with a Meinhard nebulizer and an impact bead spray chamber.

2.3.3. Sulfur analysis

Approximately 0.2 g of milled sample was weighed off and sent to the Council for Geoscience, South Africa, for sulfur analysis. No further preparation was necessary and samples were directly analyzed on an Eltra CS 800 double dual range carbon-sulfur analyzer.

3. Results

3.1. Petrography

Table 1 presents a summary of the petrographic observations made on the various samples, with representative photomicrographs shown in Fig. 4. The two sets of non-pegmatoidal Merensky reef cores (borehole SD14/90 & BH6259) correlate well with each other and will therefore be discussed together below.

3.2. Mineral chemistry

The composition of plagioclase in all units studied covers a range from labradorite (An_{70-50}) to bytownite (An_{90-70}). The composition of plagioclase in the two non-pegmatoidal Merensky reef core samples (borehole SD14/90 & BH6259) is fairly constant with an% ranging from 51 to 73 in the hangingwall, 74–82 in the chromitite layer and 76–82 in the footwall anorthosite layer (Fig. 5a and b). The An% composition for the pegmatoidal Merensky reef core (borehole 20/0252) ranges between 62 and 63 in the hangingwall pyroxenite, 73–74 for the top chromitite layer, 52–79 in the pegmatoidal layer and 71–76 for the footwall anorthosite (Fig. 5c). See electronic supplementary files for data.

The composition of orthopyroxene mostly falls within the enstatite field. In borehole SD14/90 and BH6259 (non-pegmatoidal

Merensky reefs) the compositions are generally enstatitic (En_{73-86}) with a wollastonite component between 1.18 and 4.82 mol%. The Mg# varies between 74.36 and 87.02 (Fig. 5d–e). In borehole 20/0252 (pegmatoidal Merensky reef) the composition of orthopyroxene is generally enstatitic (En_{76-80}) with a wollastonite component of up to 4.49 mol%. The Mg# varies between 77.7 and 80.76 (Fig. 5f). See electronic supplementary files for data.

Clinopyroxene occurs as inclusions or as lenses in orthopyroxene, or as oikocrysts. The composition of clinopyroxene in these units covers a range from diopside to augite. In borehole SD14/90 and BH6259 the Mg# varies between 81.74 and 89.28 (Fig. 5d–e). In borehole 20/0252 the Mg# varies between 79.36 and 88.07 (Fig. 5f). See electronic supplementary files for data.

In borehole SD14/90 and BH6259 (non-pegmatoidal Merensky reef) the chromitite stringers show Cr_2O_3 concentrations ranging from 41.35 wt% to 45.22 wt%. In borehole 20/0252 the disseminated chromite in the hangingwall pyroxenite shows Cr_2O_3 concentrations that range from 40.2 wt% to 50.21 wt%. Compact chromite in the top chromitite layer shows Cr_2O_3 concentrations of 41.45 wt%. The disseminated chromite in the pegmatoidal pyroxenite layer shows Cr_2O_3 of 38.71 wt% to 39.52 wt%. Compact chromite in the bottom chromitite layer shows Cr_2O_3 concentrations of 44.26 wt%. See electronic supplementary files and Table 2 for data.

3.3. Whole-rock geochemistry

3.3.1. Major element geochemistry

Variation in whole rock Mg# are shown in Fig. 6 a–c. In borehole SD14/90 and BH6259 (non-pegmatoidal Merensky reef) Mg# ranges between 73.33 and 81.67 for the hangingwall pyroxenite; 41.87–52.49 for the chromitite stringer and 68.81–79.12 for the footwall anorthosite. In borehole 20/0252 (pegmatoidal Merensky reef) the Mg# ranges between 71.83 and 79.65 for the hangingwall pyroxenite; 61.60 for the top chromitite stringer; 74.42–82.63 for the pegmatoidal pyroxenite layer; 75.33–78.84 for the bottom chromitite stringer and between 54.22 and 76.77 for the footwall anorthosite (see Table 3 for average whole rock major element compositions).

Fig. 6 d–f shows the variation in whole rock An% (calculated from the norm) versus borehole depth for the 3 boreholes characterized. An% ranges between 60.06 and 80.96% for the hangingwall pyroxenite; 80.38–89.65% for the chromitite stringer and 75.23–92.36% for the footwall anorthosite of borehole SD14/90 and BH6259. For borehole 20/0252 the An% ranges between 77.05 and 91.01% for the hangingwall pyroxenite; 91.21% for the top chromitite stringer, 73.49–94.08% for the pegmatoidal pyroxenite layer 82.95–83.34%, for the bottom chromitite stringer and 75.49–93.30% for the footwall anorthosite.

3.3.2. Whole rock REE geochemistry

Chondrite normalised REE diagrams for the different units in the various boreholes are shown in Fig. 7, with the data tabulated in Table 4. In borehole SD14/90 and BH6259 all the lithologies are relatively enriched in LREE with the hangingwall pyroxenite showing an average Ce/Sm_N of 1.58 & 2.07, the chromitite stringer 2.75 & 2.43 and the footwall anorthosite showing an average of 2.65 & 2.83 respectively. The rocks show very little fractionation of the HREE with the hangingwall pyroxenite showing an average Tb/Yb_N of 0.87 & 0.93, the chromitite stringer 1.53 & 1.25 and the footwall anorthosite showing slightly more fractionation with an average of 1.49 & 1.75, respectively (Fig. 7a and b). Both the chromitite layer and the footwall anorthosite show strong positive Eu anomalies. The hangingwall pyroxenite

Table 1
Summary of petrographic data for the various boreholes (SD14/90; BH6259 and 20/0252).

		Plagioclase (Plag)	Orthopyroxene (Opx)	Chromite (Chr)	Phlogopite (Phlog)	Sulfide phases (Sulf)	Acc minerals
Borehole SD14/90 and BH6259 non-pegmatoidal reef	HW	25%; intercumulus; Wedge shaped twins and lamellar twinning	65%; Sub-to-anhedral; narrowly spaced exsolution lamellae of cpx; some are interpenetrating on faces orientated at a high angle to the vertical (Fig. 4a)		4%; brown to light greenish brown are interstitial to pyx	5% intergrowths of phases like pyrr, pent and chalc	1% cpx (Fig. 4e)
	Chr layer	20%; Intercumulus; wedge shaped twins	5%; anhedral; patches between chr	65% modal chr; shape from cubic to amoeboidal (Fig. 4b)	4%; interspersed between chr (Fig. 4b)	5%; visible throughout thin section; in some chr sulf droplets are preserved (Fig. 4d)	1% cpx
	FW	90%; cumulus; lath shaped (Fig. 4f); few show zoning;	5%; anhedral opx towards the base;		3% anhedral; interstitial to plag	2%; occur between plag laths; other are poikilitically enclosed	
Borehole 20/0252 Pegmatoidal layer	HW	30%; Intercumulus; wedge shaped deformation twins	55%; subhedral; exsolution lamellae of cpx; opx in contact with serp show alteration; on rim altered to amph	2%; Interstitial to poikilitic chromite	4%; Interstitial to poikilitic phlog	8%; finer sulf grains occur interspersed within the serpentine veins	1% cpx; talc
	Top Chr layer	8%; intercumulus	20%; anhedral; with narrowly spaced exsolution lamellae	55%; shape round to amoeboidal	5% showing brown pleochroism	10%; finer sulf phases are present;	2% cpx
	Pegma-toidal layer	15% occur as both oikocrysts and intercumulus phase	55% Large oikocrysts, some altered to amph; some contain exsolution lamellae (Fig. 4c).	7% Interstitial to poikilitic chr	5% showing brown to light green pleochroism	5% large serp veins with smaller sulf interspersed; large grains consisting of different phases occur.	13% cpx; amph; talc; serp (Fig. 4c)
	Bottom Chr layer	35%; Large oikocrysts; wedge shaped deformation twins	10%; Oikocrysts with exsolution lamellae of cpx	45%; shape ranges from cubic to amoeboidal	3%; interspered between chr grains	5%; anhedral grains	2% cpx
	FW	85%; Cumulus; lath to tabular shaped	10% interstitial opx		3%; showing pleochroism	2%; finer sulf phases	
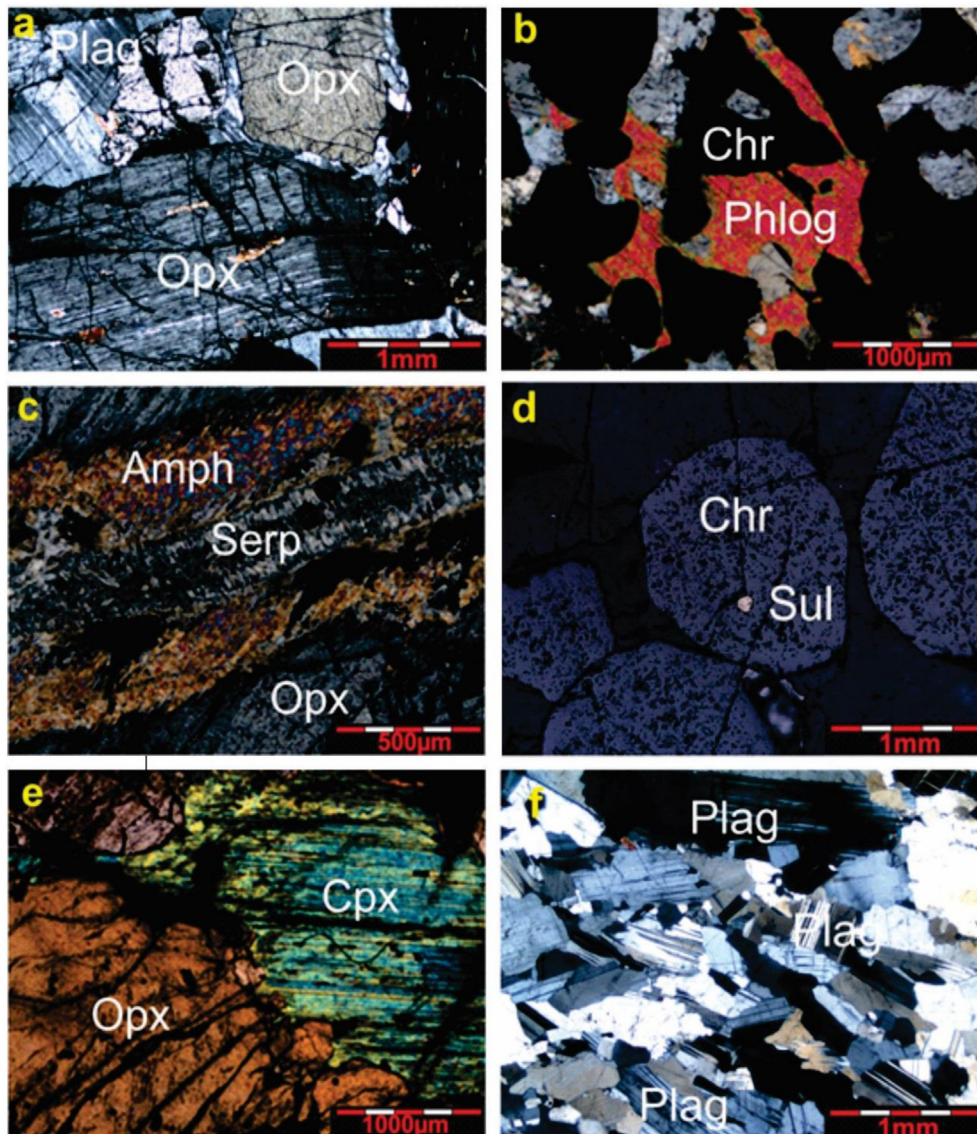
Fig. 4. Photomicrographs of: (a) Orthopyroxene interpenetrating on faces orientated at a high angle to the vertical and orthopyroxene with narrowly spaced exsolution lamellae from the hangingwall of borehole SD14/90, under cross-polarized light. (b) Phlogopite interspersed between chromite in the chromitite layer of borehole SD14/90, under cross-polarized light. (c) Veins of serpentine penetrating orthopyroxene on the side in the pegmatoidal layer of borehole 20/0252, orthopyroxene showing alteration, under cross-polarized light. (d) Sulfide grain visible in a chromite grain that displays a negative crystal shape imposed by the crystal structure of the host chromite in the chromitite stringer of borehole BH6259, under reflected light. (e) A large clinopyroxene grain partially including orthopyroxene in the hangingwall of borehole BH6259, under cross-polarized light. (f) Lath to tabular shaped plagioclase in the footwall of borehole BH6259, photomicrograph under cross-polarized light. Cpx, clinopyroxene; Plag, plagioclase; Chr, chromite; Sul, sulfide; Opx, orthopyroxene; Phlog, phlogopite, Serp, serpentine; Amph, amphibole.

shows negative Eu anomalies (Fig. 7a and b).

In borehole 20/0252 the hangingwall pyroxenite and top chromitite stringer show average Ce/Sm$_N$ of 1.20 and 0.87, respectively. The pegmatoidal pyroxenite layer, bottom chromitite stringer and the footwall anorthosite are relatively enriched in LREE with the pegmatoidal pyroxenite layer showing an average Ce/Sm$_N$ of 2.21, the bottom chromitite stringer 2.02 and the footwall anorthosite 2.89. The rocks show very little fractionation of the HREE with the hangingwall pyroxenite showing an average Tb/Yb$_N$ of 0.67, the top chromitite stringer 1.35, the pegmatoidal pyroxenite layer 0.86 and the bottom chromitite stringer 0.67. The footwall anorthosite shows slightly more fractionation with an average Tb/Yb$_N$ of 1.86. Eu shows positive anomalies in the footwall anorthosite, and bottom chromitite layer with negative anomalies in the top chromitite layer and in the hangingwall pyroxenite (Fig. 7c).

3.3.3. PGE geochemistry (ICP-MS)

Whole rock PGE data for the different units in the three boreholes are given in Table 5 and is graphically depicted in Fig. 8.

In borehole SD14/90: Pt + Pd + Rh in the hangingwall pyroxenite is 11 ppm, in the chromitite stringer (NP5-6) 66 ppm and in the first 6 cm of the anorthosite footwall (NP7-9) 12 ppm, after which it drops to <0.1 ppm.

In borehole BH6259: the average Pt + Pd + Rh in the hangingwall pyroxenite about 8 cm above the chromitite stringer is < 1 ppm; the next 8 cm averages at 9 ppm. In the chromitite stringer (N98) the average is 67 ppm and in the anorthosite footwall <1 ppm.

In borehole 20/0252: the top chromitite stringer (P12) has an average Pt + Pd + Rh of 22 ppm and the bottom chromitite stringer (P47 − P48) 3 ppm. The hangingwall pyroxenite has an
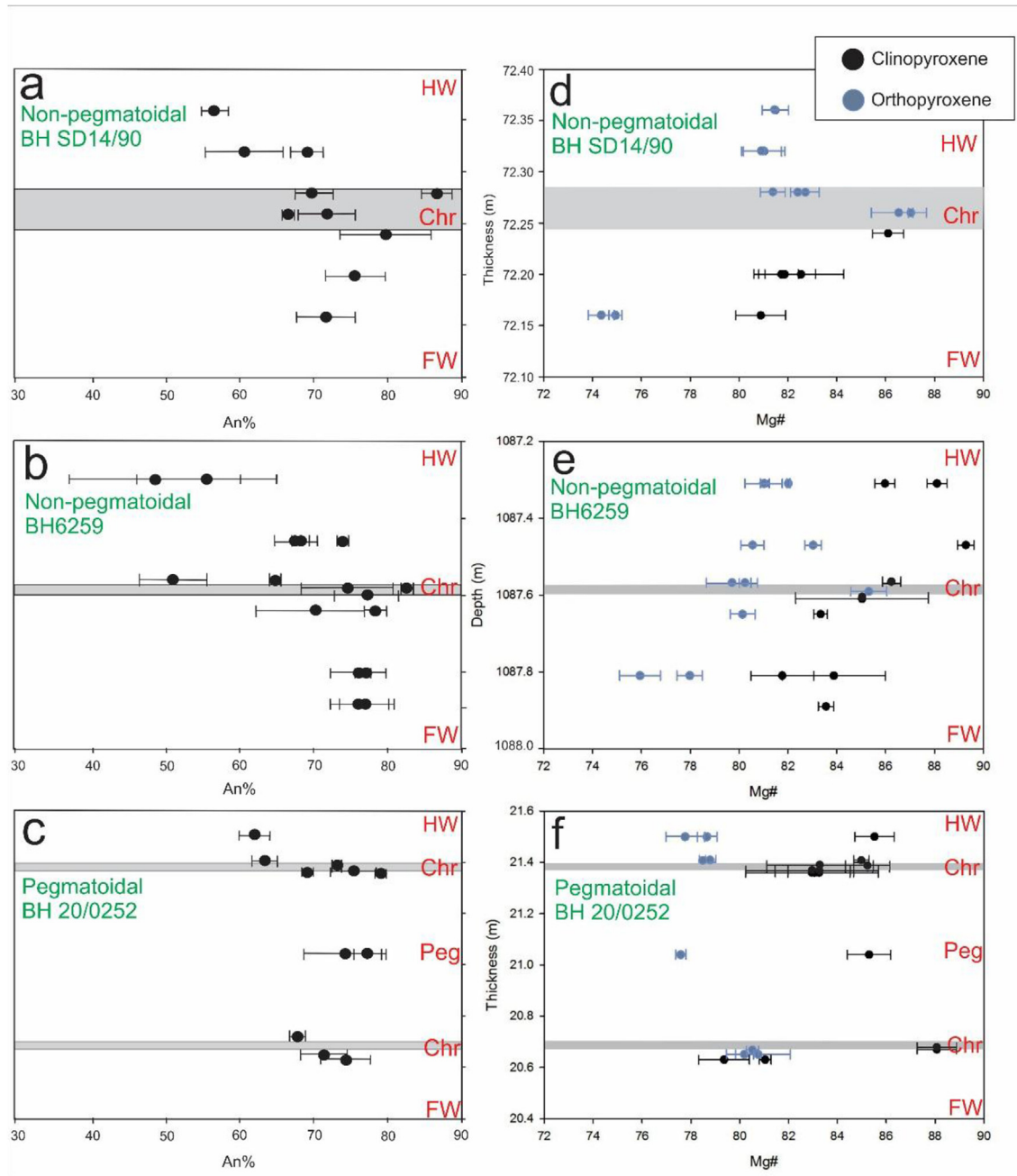
Fig. 5. a–c: Plot of borehole depth/thickness versus An% (with error bars indicating the RSD) in plagioclase of boreholes a) SD14/90; b) BH6259; c) 20/0252. Fig. 5 d–f: Plot of borehole depth/thickness versus Mg# (with error bars indicating the RSD) in orthopyroxene and clinopyroxene of borehole d) SD14/90; e) BH6259; f) 20/0252.

Table 2
Average chromite composition in the various chromitite layers for the various boreholes. Major element oxides in wt%. (Cr/(Cr + Al) calculated using molar values.

	SiO_2	CaO	TiO_2	Al_2O_3	FeO	Fe_2O_3	ZnO	MnO	NiO	V_2O_3	MgO	Cr_2O_3	Total	Mg#	Cr/(Cr + Al)	Cr/(Cr + Fe^{total})
Top Chr layer	0.12	0.01	2.74	12.38	29.30	8.14	0.19	0.28	0.25	0.65	5.68	41.45	100.38	58.07	0.69	0.57
Bottom Chr layer	0.12	0.02	1.02	16.61	24.16	6.71	0.05	0.27	0.18	0.33	7.17	44.26	100.23	67.92	0.64	0.59
Single N 98	0.04	n.d.	0.99	19.52	23.45	6.52	0.17	0.27	0.16	0.29	8.09	41.66	100.52	71.11	0.59	0.57
Top (5-6NP)	0.07	0.01	0.92	18.74	23.98	6.66	0.11	0.29	0.15	0.25	7.87	41.55	99.94	70.08	0.60	0.52
Bottom (7NP)	0.101	0.08	0.82	18.05	23.52	6.53	0.21	0.31	0.15	0.24	7.48	44.27	101.09	69.42	0.62	0.58

average Pt + Pd + Rh of 16 ppm in a zone up to 4 cm above the top chromitite stringer, after which levels drop to <3 ppm. Mineralization in the pegmatoidal pyroxenite layer is concentrated in the top 40 cm, just below the top chromitite (average Pt + Pd + Rh 9.34 ppm) with the bottom 28 cm being essentially barren. The footwall anorthosite shows no PGE
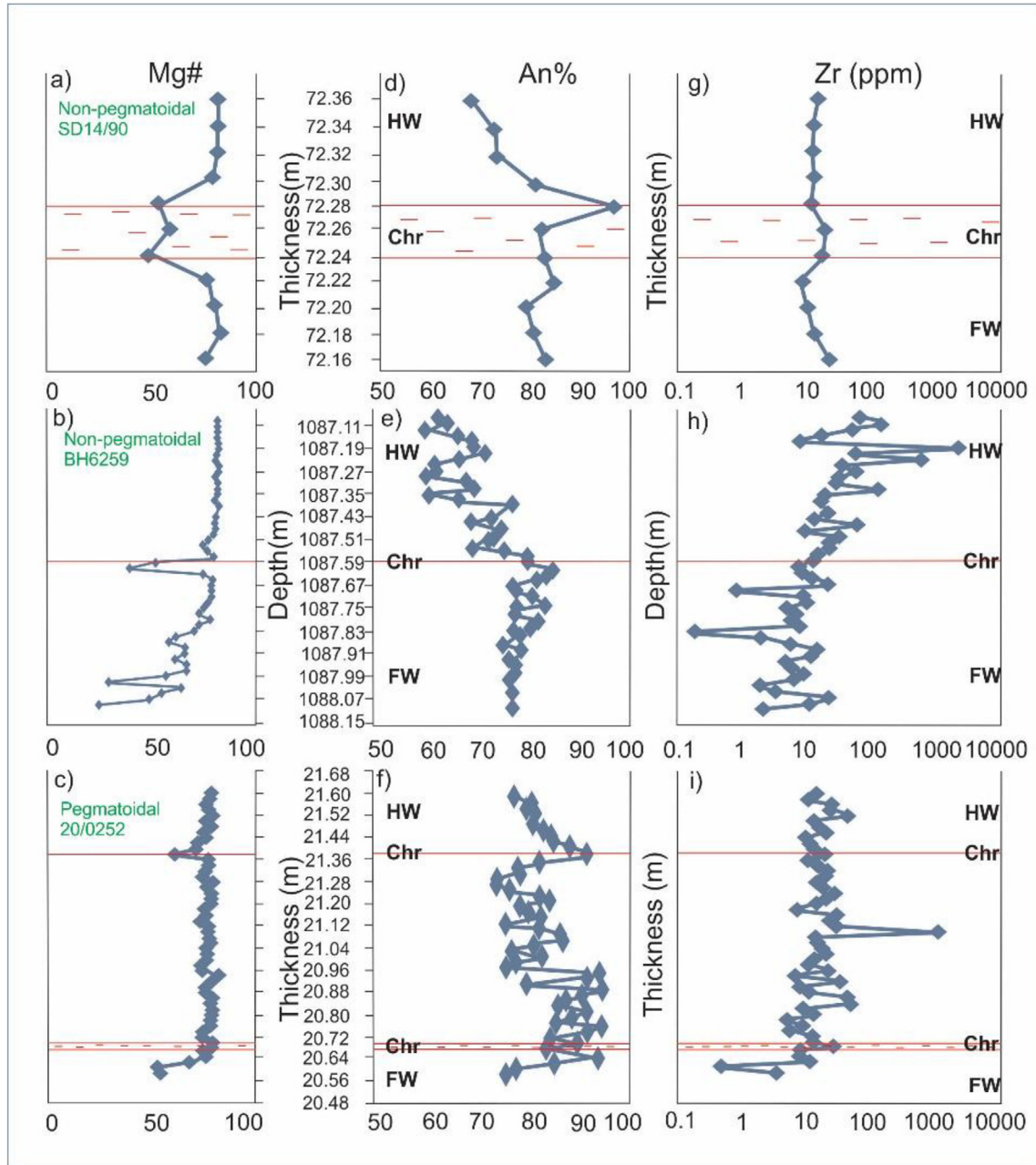
Fig. 6. (a-c) Variation in whole rock Mg# of borehole: a) SD14/90; b) BH6259 and c) 20/0252. (d−f) Variation in whole rock normative An% of borehole d) SD14/90; e) BH6259 and f) 20/0252. Variation in whole rock Zr (ppm) of borehole g) SD14/90; h) BH6259 and i) 20/0252. Position of chromitite stringers indicated by lines.

(average Pt + Pd + Rh < 0.01 ppm) mineralization.

As can be seen from Fig. 8, the PGE trends follow the Cr trend (the black curve) very closely (especially in the chromitite stringer) in the two non-pegmatoidal Merensky reef intersections (borehole SD14/90 and borehole BH6259). There is a slight indication of PGE trends following the S trend in the footwall anorthosite of these two boreholes. In the pegmatoidal Merensky reef (borehole 20/0252) the trend is slightly more irregular with the PGE trend following the Cr trend in the top and bottom chromitite stringers and in the footwall anorthosite. In the hangingwall pyroxenite and parts of the pegmatoidal pyroxenite layer the PGE trends follow the S trend. Cu shows a strong correlation with S in all three cases. The Cu/Pd ratio shows the exact opposite trend as the Cr trend, especially in the non-pegmatoidal Merensky reef intersections.

4. Discussion

4.1. Distribution of PGE across Merensky reef types

Lee (1983) and Lee and Tredoux (1986), divided the ore metals from the Merensky reef into two groups. 1) Ni, Cu, Au and Pd, and 2) Ir, Rh, Pt and Cr. It was suggested that Pd and Au were controlled by sulfides (supported by Barnes and Maier, 2002) and that Pt, Ir and Rh were controlled by platinum group minerals (PGM) or spinel. These models can be tested by the observations made in this study.

In all three Merensky intersections studied, both Pt and Pd concentrations show locally elevated concentrations in the vicinity of chromitite layers. For borehole SD14/90 that intersected non-pegmatoidal reef, the association between Pt, Pd and Cr appears

Table 3
Average whole rock geochemistry (major element oxides and element ratios) in the different lithologies of the different boreholes obtained from ICP-MS analysis. Major element oxides in wt%. Cr/(Cr + Al) and Cr/(Cr + Fe^{total}) calculated using molar values.

	Borehole SD14/90			Borehole BH6259			Borehole 20/0252				
	HW	Chr layer	FW	HW	Chr layer	FW	HW	Top Chr layer	Peg layer	Bottom Chr layer	FW
SiO$_2$	49.31	28.74	47.79	51.55	27.73	48.54	49.39	35.08	48.96	45.44	47.95
TiO$_2$	0.25	0.56	0.08	0.26	0.62	0.06	0.23	1.08	0.16	0.17	0.04
Al$_2$O$_3$	5.75	20.21	28.35	5.69	17.87	28.08	3.48	6.53	6.69	8.94	28.19
Fe$_2$O$_3$	3.01	3.91	0.47	2.41	3.98	0.47	3.07	4.06	2.56	2.54	0.24
FeO	10.85	14.06	1.68	8.69	14.32	1.71	11.04	14.60	9.21	9.15	0.87
MnO	0.22	0.18	0.04	0.20	0.19	0.03	0.26	0.26	0.20	0.21	0.02
MgO	22.98	9.27	3.40	24.09	10.62	3.16	25.61	16.40	22.60	21.85	1.53
CaO	4.30	5.64	15.80	3.82	4.97	14.79	3.54	9.01	4.64	5.79	17.06
Na$_2$O	0.51	0.64	1.99	0.61	0.67	2.08	0.20	0.18	0.39	0.49	2.16
K$_2$O	0.03	0.11	0.14	0.30	0.11	0.14	0.05	0.08	0.12	0.03	0.38
P$_2$O$_5$	0.01	0.02	0.03	0.08	0.01	0.02	0.01	n.d.	0.02	0.02	0.02
Cr$_2$O$_3$	1.31	14.77	0.11	0.40	18.55	0.06	1.04	11.55	0.32	3.36	0.03
NiO	0.66	0.31	0.07	0.37	0.45	0.07	0.64	0.96	0.41	0.11	0.03
LOI	0.49	n.d.	0.31	0.27	n.d.	0.39	0.44	0.03	2.58	1.14	0.97
Total	100.89	99.32	100.43	99.69	100.95	99.78	100.23	101.45	99.89	100.26	99.58
Element ratios											
Mg#	75.15	47.05	72.54	79.88	51.43	63.50	76.76	61.60	77.59	77.09	63.10
An%	73.65	88.10	81.52	68.60	80.38	78.89	82.70	91.21	83.37	83.15	82.80
Cr/(Cr + Fe^{total})	0.07	0.45	0.05	0.14	0.49	0.02	0.20	0.75	0.12	0.55	0.10
Cr/(Cr + Al)	0.11	0.32	n.d.	0.03	0.41	0.01	0.14	0.54	0.05	0.20	n.d.

much more significant that the association between Pt, Pd and sulfur, the latter having elevated concentrations immediately below the chromitite layer as is apparent from Fig. 8a. The same holds true for the non-pegmatoidal reef intersection as exposed in borehole BH6259 (Fig. 8b), although here, sulfide enrichment as exemplified by elevated sulfur and copper concentrations appear in the samples overlying the chromitite layer, with once again the highest Pt and Pd values recorded within the chromitite layer itself. Locally elevated Pt and Pd concentrations occur at or close to both the bottom and top chromitite layers of the pegmatoidal reef as exposed in borehole 20/0252, with again a much stronger correlation between elevated Pt, Pd and Cr as opposed to elevated Pt, Pd and sulfur (Fig. 8c).

On the basis of these observations, we have to conclude that the primary association within the Merensky reef is between PGE and Cr and not between PGE and sulfur, as has been suggested to be the case by numerous authors. This realisation lends credence to the suggestion by Tredoux et al. (1995) for the existence of PGE clusters that may be physicochemically associated with spinel-type phases like chromite and that can act as nucleation sites for chromite during crystallization thereof at magmatic temperatures.

4.2. A model for the formation of the pegmatoidal Merensky reef

We envisage that the pegmatoidal Merensky reef was formed by the introduction of a chromite-laden basal flow from a deeper staging chamber onto an anorthositic crystal mush that today forms the footwall to the Merensky reef. Latypov et al. (2018) has shown that it is possible to create a chromite-only saturated melt as a result of pressure reduction during magma ascent. We propose that chromite fractionation occurred within a staging chamber underlying the presently exposed Bushveld Complex, with PGE clusters being incorporated into the chromite before being introduced into the Bushveld Complex magma chamber. The chromite crystals settled to the base of this flow, becoming lodged between plagioclase crystals of the anorthosite footwall, explaining both the elevated PGE content of the bottom chromitite layer and the positive Eu anomaly of this layer. This bottom flow subsequently crystallised, essentially as a sill, to produce a feldspathic pyroxenite

layer with the thin, aforementioned chromitite layer at its base. Because the magma that produced this layer did not experience plagioclase fractionation and because it is envisaged to have crystallised largely in situ, at least close to feeder zones, it shows no evidence for either a positive or negative Eu anomaly. The resident magma was displaced upwards when this basal flow was introduced into the magma chamber and did not undergo significant mixing with the basal flow in the proximity of feeder zones, although lateral expansion of the flow is thought to have resulted in more pronounced mixing in distal areas, the reason for which will be expanded upon below. It should be remembered at this stage that the resident magma was fractionating plagioclase as it was responsible for the deposition of the anorthosite footwall.

A second chromite-laden basal flow, was subsequently introduced into the chamber, again displacing the resident magma upwards. This flow deposited another layer of PGE-enriched chromite onto the earlier introduced "sill", reconstituting the latter to form a pegmatoidal feldspathic pyroxenite as explained by Cawthorn and Boerst (2006). The second magma pulse, however, is thought to have partially mixed with the resident magma, which previously underwent plagioclase fractionation, forming the Merensky pyroxenite, with a negative Eu anomaly, as the hangingwall to the pegmatoidal Merensky reef. Such an interpretation is also consistent with the presence of much more sodic plagioclase in the hangingwall compared to lower down in the succession.

4.3. Relationship between the pegmatoidal and non-pegmatoidal Merensky reef

A schematic diagram showing the mineral chemistry of chromitite in the various chromitite layers of the pegmatoidal and non-pegmatoidal reef intersections is given in Fig. 9 with the trivalent cations present in chromite shown in a ternary diagram in Fig. 10. On the basis of what is shown in Fig. 10, we conclude that the lower chromitite layer of the pegmatoidal layer is a correlate of the single chromitite layer as seen in non-pegmatoidal reef intersections. This is contrary to what was found to be the case at Marikana by Cawthorn and Wansbury (2014), who concluded that the upper chromitite layer of the pegmatoidal reef was a correlate of the
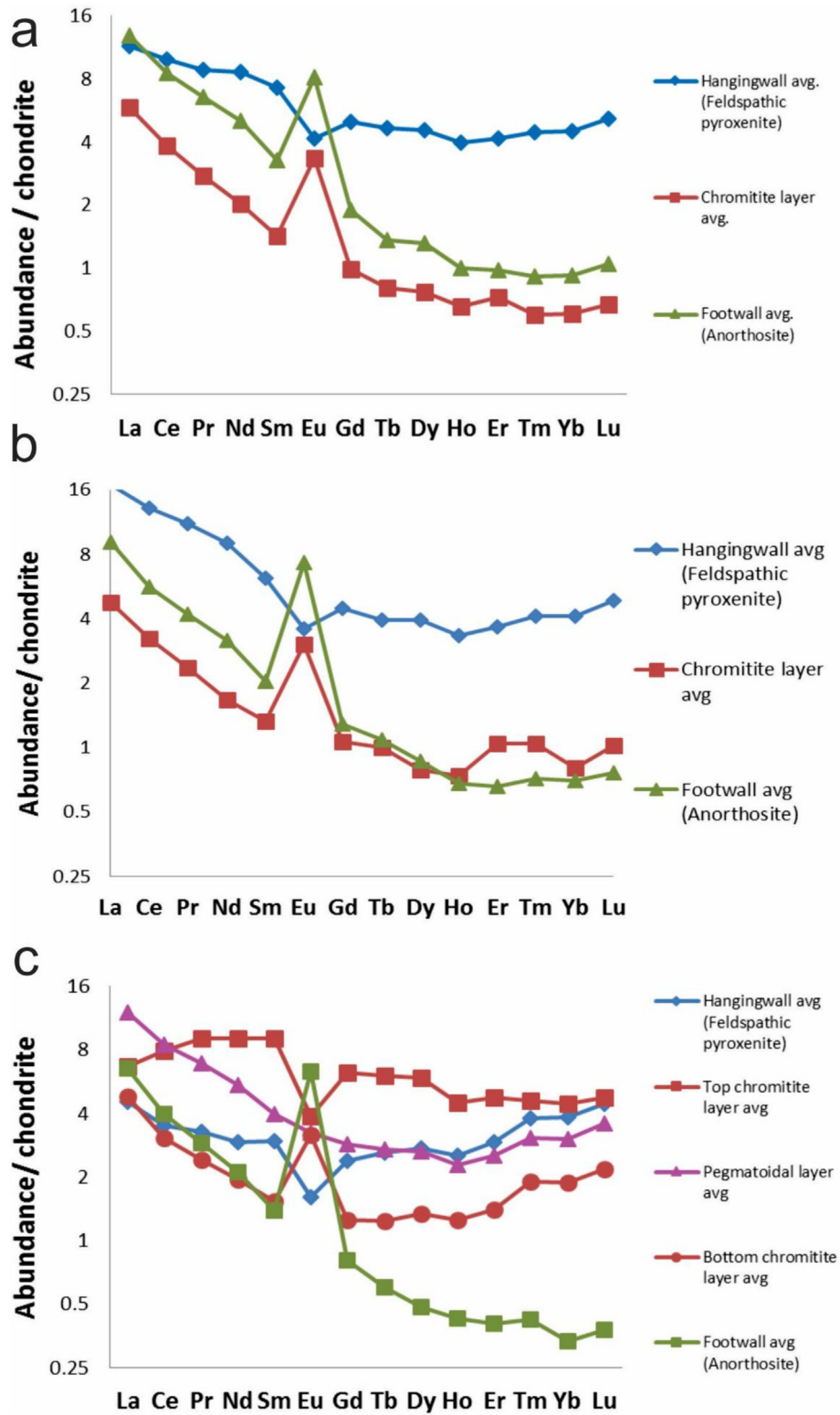
Fig. 7. Chondrite-normalised REE diagrams for a) borehole SD14/90; b) borehole BH6259 and c) borehole 20/0252. C1 chondrite normalised values are from Lodders (2003).

Table 4
Average whole rock REE composition of the various boreholes obtained from ICP-MS analysis. REE concentrations in ppm.

	Borehole SD14/90			Borehole BH6259			Borehole 20/0252				
	HW	Chr layer	FW	HW	Chr layer	FW	HW	Top chr layer	Peg layer	Bottom chr layer	FW
La	2.05	1.36	2.97	3.93	1.11	2.11	1.05	1.56	2.79	1.12	1.52
Ce	4.27	2.39	5.30	8.17	2.01	3.48	2.18	4.94	5.27	1.89	2.46
Pr	0.55	0.26	0.61	1.03	0.22	0.39	0.30	0.85	0.64 0.22	0.27	
Nd	2.43	0.93	2.29	4.11	0.76	1.44	1.33	4.14	2.50	0.89	0.96
Sm	0.65	0.21	0.47	0.89	0.19	0.30	0.43	1.32	0.58	0.22	0.20
Eu	0.19	0.18	0.44	0.20	0.17	0.40	0.09	0.21	0.18	0.17	0.35
Gd	0.65	0.20	0.38	0.88	0.21	0.25	0.48	1.24	0.57	0.25	0.16
Tb	0.12	0.03	0.05	0.14	0.04	0.04	0.09	0.21	0.10	0.04	0.02
Dy	0.78	0.18	0.31	0.94	0.19	0.21	0.65	1.40	0.63	0.32	0.12
Ho	0.16	0.04	0.06	0.19	0.04	0.04	0.14	0.25	0.13	0.07	0.02
Er	0.51	0.12	0.16	0.59	0.17	0.11	0.47	0.77	0.41	0.23	0.07
Tm	0.09	0.01	0.02	0.10	0.02	0.02	0.09	0.11	0.07	0.05	0.01
Yb	0.60	0.10	0.15	0.67	0.13	0.11	0.63	0.72	0.49	0.31	0.05
Lu	0.10	0.02	0.02	0.12	0.02	0.02	0.11	0.11	0.09	0.05	0.01

Table 5
Average whole rock PGE content of the various boreholes obtained from ICP-MS analysis. PGE concentrations in ppm, S and Cr in wt%.

	Borehole SD14/90			Borehole BH6259			Borehole 20/0252				
	HW	Chr layer	FW	HW	Chr layer	FW	HW	Top chr layer	Peg layer	Bottom chr layer	FW
Os	0.08	0.86	0.01	0.08	1.11	0.01	0.07	0.38	0.10	0.06	n.d.
Ir	0.18	1.42	0.01	0.09	1.67	0.01	0.13	0.60	0.16	0.07	n.d.
Ru	0.91	7.35	0.09	0.53	8.70	0.04	0.66	3.16	0.84	0.47	n.d.
Rh	0.56	4.47	0.05	0.20	5.08	0.02	0.35	1.56	0.39	0.14	n.d.
Pt	6.81	42.99	0.68	2.62	51.40	0.36	5.41	16.54	3.66	1.03	0.01
Pd	2.71	6.58	0.44	1.09	10.35	0.25	1.33	4.11	1.55	0.12	n.d.
Cr	0.77	10.16	0.06	0.34	12.76	0.07	1.09	7.95	0.22	2.31	0.01
S	1.15	0.43	0.02	0.92	0.45	0.06	1.17	0.58	0.40	n.d.	0.01

single layer in non-pegmatoidal reef intersections. This was interpreted to be a reflection of the idea that, where non-pegmatoidal reef exists, both the Merensky pegmatoid and lower chromitite layer were eroded by a new influx of magma that precipitated the upper/single chromitite layer. Clearly an erosional model would not be capable of explaining the results at IPM.

We propose that where non-pegmatoidal reef is encountered at IPM, non-deposition rather than erosion was responsible for the lack of pegmatoid and an upper chromitite layer, specifically non-deposition of the second magma influx that was referred to in section 4.2 above. We envisage that non-deposition may have occurred in areas further away from feeders supplying the second magma influx. In areas proximal to feeder zones, the second magma influx flowed over the first magma influx that deposited the lower chromitite layer, depositing a second chromitite layer on top and reconstituting the underlying layer to pegmatoid. In areas not covered by the second magma influx, we would therefore only expect a single chromitite layer overlain by a feldspathic pyroxenite of normal grain size, as is observed for non-pegmatoidal reef intersections.

The implication of the above model is that the feldspathic pyroxenite overlying the chromitite layer in non-pegmatoidal reef intersections is the lateral correlate of the Merensky pegmatoid, albeit with a mixed-in component of resident magma that was responsible for the deposition of the anorthositic footwall to the Merensky Reef. Such a model accounts effectively for the negative Eu anomaly of the non-pegmatoidal reef hanging wall as shown in Fig. 7 a and b.

A further aspect of our dataset needs clarification considering our proposed model, *viz.* the lower PGE concentrations of the lower chromitite (in pegmatoidal intersections) compared to that of the single chromitite (in non-pegmatoidal intersections), in light of the fact that these two are thought to be correlates. We propose that in pegmatoidal reef intersections, remobilization of PGEs may have occurred during reconstitution of the reef, thereby lowering the PGE content of the lower chromitite. Where reconstitution of the reef did not happen, in areas further away from magma feeder zones, the "original" PGE content of the chromitite layer was retained.

5. Conclusions

Our high-resolution mineralogical and geochemical study of non-pegmatoidal and pegmatoidal Merensky reef intersections at Impala Platinum Mines have made the following important findings:

i) The lower chromitite layer of pegmatoidal reef intersections is the lateral correlate of the single chromitite layer of non-pegmatoidal reef intersections. The PGE content of the former is, however, lower than the latter due to remobilization of PGEs during the formation of the pegmatoid.

ii) PGEs show a much more intimate association with Cr than with sulfur (or Cu as a proxy for sulfides), which we interpret to be a reflection of the physicochemical incorporation of PGEs in chromite in a staging chamber prior to emplacement of chromite-laden slurries into the Bushveld Complex magma chamber to give rise to both chromitite layers of the pegmatoidal Merensky reef.
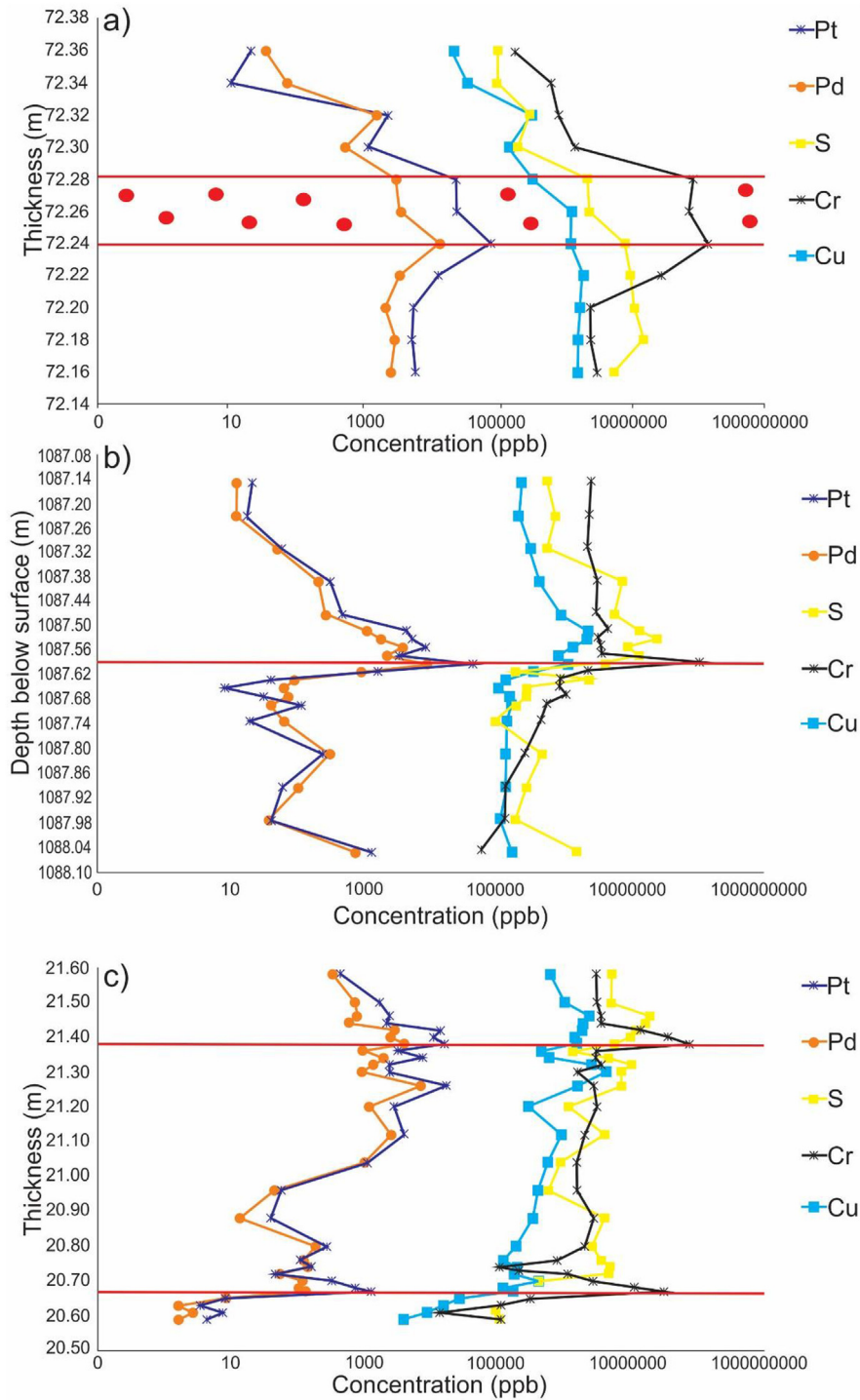
Fig. 8. Pt, Pd, Cr and S values vs borehole depth for borehole a) SD14/90; b) BH6259 and c) 20/0252. The rest of the PGEs show trends similar to those of Pt and Pd. Chromitite stringers indicated by a red line. (For interpretation of the references to colour in this figure legend, the reader is referred to the Web version of this article.)

iii) The Merensky pegmatoid was formed through reconstitution of an original feldspathic pyroxenite that crystallised largely *in situ* from a sill-like basal flow that did not undergo significant mixing with resident magma, as a result of a second basal flow that was extruded on top of the first and that also deposited the second chromitite layer. This second flow mixed with resident magma that deposited the anorthositic footwall to the Merensky reef, resulting in negative Eu anomalies as seen in the hanging wall to the Merensky pegmatoid.

iv) The feldspathic pyroxenite overlying the chromitite layer in non-pegmatoidal reef intersections represent material
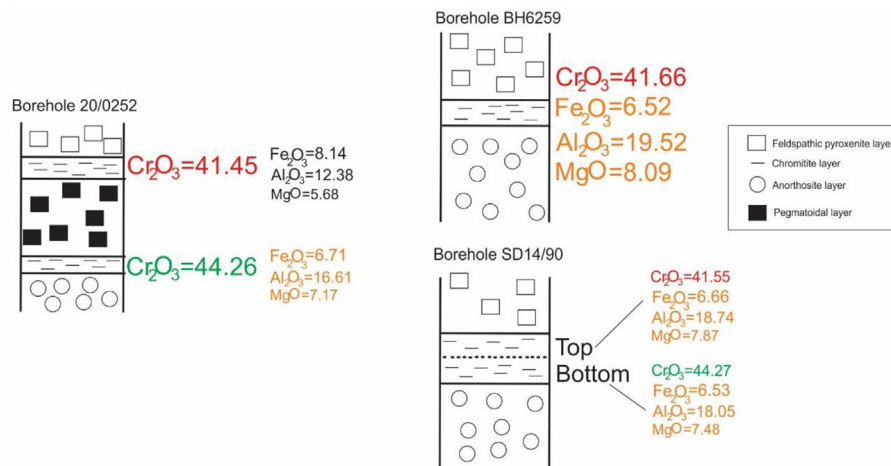
Fig. 9. a) Schematic diagram of the pegmatoidal Merensky reef, borehole 20/0252 (with two chromitite stringers); the non-pegmatoidal reef (one chromitite stringer) borehole BH6259 and the non-pegmatoidal reef (one chromitite stringer) borehole SD14/90 showing the average chromite composition in the various chromitite layers.
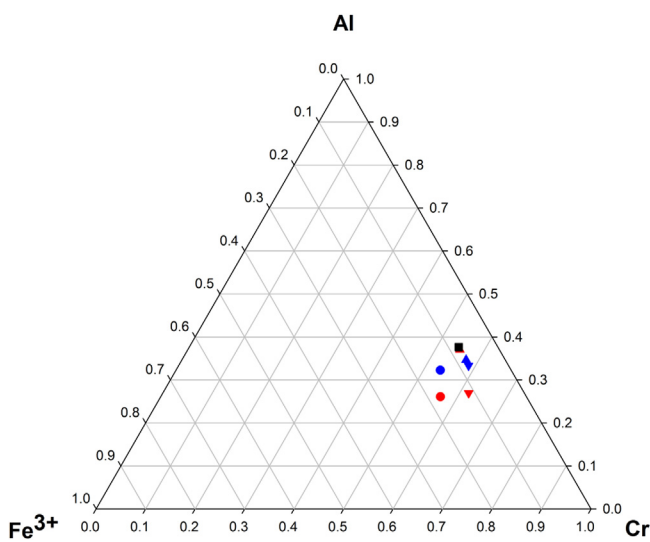
Fig. 10. Cr, Al and Fe^{3+} ternary showing chromite compositions with the data of Vukmanovic et al. (2013) included. Red symbols are for upper chromitite layers and blue symbols for lower chromitite layers. Circles = Vukmanovic et al. (2013), triangles = non-pegmatoidal reef (borehole SD14/90), black box = non-pegmatoidal reef (borehole BH6259), inverted triangles = pegmatoidal reef (borehole 20/0252). (For interpretation of the references to colour in this figure legend, the reader is referred to the Web version of this article.)

crystallised from the first basal flow mixed with resident magma and may therefore be laterally correlated with the Merensky pegmatoid.

v) Non-deposition as opposed to erosion is responsible for the differences between the pegmatoidal and non-pegmatoidal reef intersections at IPM.

Appendix A. Supplementary data

Supplementary data related to this article can be found at https://doi.org/10.1016/j.jafrearsci.2018.04.014.

References

Barnes, S.J., Maier, W.D., 2002. Platinum-group element distributions in the Rustenburg layered suite of the Bushveld complex, South Africa. In: Cabri, L.J. (Ed.), The Geology, Geochemistry, Mineralogy and Mineral Beneficiation of Platinum Group Elements. Canadian Institute of Mining, Metallurgy and Petroleum, pp. 431–455. Special vol. 54.

Boudreau, A.E., Meurer, W.P., 1999. Chromatographic separation of the platinum-group elements, gold, base metals and sulfur during degassing of a compacting and solidifying crystal pile. Contrib. Mineral. Petrol. 134, 174–185.

Campbell, I.H., Naldrett, A.J., Barnes, S.J., 1983. A model for the origin of the platinum-rich sulfide horizons in the Bushveld and Stillwater Complexes. J. Petrol. 24, 133–165.

Cawthorn, R.G., 1999. The platinum and palladium resources of the Bushveld complex. South Afr. J. Sci. 95, 481–489.

Cawthorn, R.G., 2005. Stratiform PGE deposits in layered intrusions. Can. Mineral. 35, 57–73.

Cawthorn, R.G., 2010a. Geological interpretations from the PGE distribution in the Bushveld Merensky and UG2 chromitite reefs. J. S. Afr. Inst. Min. Metall 107, 57–70.

Cawthorn, R.G., 2010b. The platinum group element deposits of the Bushveld complex in South Africa. Platin. Met. Rev. 54, 205–215.

Cawthorn, R.G., Boerst, K., 2006. Origin of the pegmatitic pyroxenite in the Merensky unit, Bushveld complex, South Africa. J. Petrol. 47 (8), 1509–1530.

Cawthorn, R.G., Eales, H.V., Walraven, F., Uken, R., Watkeys, M.K., 2006. The Bushveld complex. In: Johnson, M.R., Anhaeusser, C.R., Thomas, R.J. (Eds.), Geology of South Africa. Geological Society of South Africa, pp. 261–281.

Cawthorn, R.G., Lee, C.A., Schouwstra, R., Mellowship, P., 2002b. Relations between PGE and PGM in the Bushveld complex. Can. Mineral. 40, 311–328.

Cawthorn, R.G., Merkle, R.K.W., Viljoen, M.J., 2002a. Platinum-group element deposits in the Bushveld complex, South Africa. In: Cabri, L.J. (Ed.), The Geology, Geochemistry and Mineral Beneficiation of Platinum Group Elements. Canadian Institute of Mining, Metallurgy and Petroleum, pp. 389–425. Special vol. 54.

Cawthorn, R.G., Wansbury, N., 2014. Formation of the chromitite layers of the Merensky unit, Bushveld complex. Abstract volume − 21st General meeting of IMA South Africa 2014. Available online at: www.ima2014.co.za/.../IMA2014%20ABSTRACT%20VOLUME_2.pdf.

Clarke, B., Uken, R., Reinhardt, J., 2009. Structural and compositional constraints on the emplacement of the Bushveld complex, South Africa. Lithos 111, 21–36.

Davey, S.R., 1992. Lateral variation within the upper critical zone of the Bushveld complex on the farm rooikoppies 297 JQ, Marikana, South Africa. S. Afr. J. Geol. 95 (3/4), 141–149.

Eales, H.V., Cawthorn, R.G., 1996. The Bushveld complex. In: Cawthorn, R.G. (Ed.), Layered Intrusions. Elsevier, p. 531. Developments in Petrology. 15.

Huber, H., Koeberl, C., McDonald, I., Reimold, W.U., 2001. Geochemistry and

petrology of Witwatersrand and Dwyka diamictites from South Africa: search for an extraterrestrial component. Geochem. Cosmochim. Acta 65 (12), 2007—2016.

Latypov, R., Chistyakova, S., Page, A., Hornsey, R., 2016. Field evidence for the in situ crystallization of the Merensky reef. J. Petrol. 56 (12), 2341—2372.

Latypov, R., Costin, G., Chistyakova, S., Hunt, E.J., Mukherjee, R., Naldrett, T., 2018. Platinum-bearing chromite layers are caused by pressure reduction during magma ascent. Nat. Commun. 9. Article #462.

Lee, C.A., 1983. Trace and platinum-group element geochemistry and the development of the Merensky unit of the western Bushveld complex. Miner. Deposita 18 (2), 173—190.

Lee, C.A., Tredoux, M., 1986. Platinum-group element abundances in the lower and the lower Critical zones of the Eastern Bushveld complex. Econ. Geol. 81, 1087—1095.

Leeb-du Toit, A., 1986. The Impala platinum Mines. In: Anhaeusser, C.R., Maske, S. (Eds.), Mineral deposits of Southern Africa, vol. 2. Geological Society of South Africa, Johannesburg, pp. 1091—1106.

Lodders, K., 2003. Solar system abundances and condensation temperatures of the elements. Astrophys. J. 591, 1220—1247.

Maier, W.D., Barnes, S.-J., Groves, D.I., 2013. The Bushveld Complex, South Africa: formation of platinum, palladium, chrome- and vanadium rich layers via hydrodynamic sorting of a mobilized cumulate slurry in a large, relatively slowly cooling, subsiding magma chamber. Miner. Deposita 48, 51—56.

McDonald, I., Holwell, D.A., 2011. Geology of the Northern Bushveld complex and the setting and genesis of the Platreef Ni-Cu-PGE deposit. Econ. Geol. 17, 297—327.

McDonald, I., Viljoen, K.S., 2006. Platinum-group element geochemistry of mantle eclogites: reconnaissance study of xenoliths from the Orapa kimberlite, Botswana. Appl. Earth Sci. (Trans. Inst. Min. Metall. B) 115 (3), 81—93.

SACS, 1980. Bushveld complex. In: K.L.E (Ed.), The Stratigraphy of South Africa, Part I, Lithostratigraphy of the Republic of South Africa, South 221 West Africa/Namibia and the Republics of Bophuthatswana, Transkei and Venda. Geological Survey of South Africa, pp. 223—231.

Scoon, R.N., Mitchell, A.A., 2009. Discovery and Geology of the platinum group element deposits of the Bushveld Complex, South Africa. SEG Newsl. 78, 13—19.

Tredoux, M., Lindsay, N.M., Davies, G., McDonald, I., 1995. The fractionation of platinum-group elements in magmatic systems, with the suggestion of a novel causal mechanism. S. Afr. J. Geol. 98 (2), 157—167.

Viljoen, M.J., Hieber, R., 1986. The Rustenburg section of Rustenburg platinum Mines limited, with reference to the Merensky reef. In: Anhaeusser, C.R., Maske, S. (Eds.), Mineral deposits of Southern Africa, vol. 2. Geological Society of South Africa, pp. 1107—1134.

Vukmanovic, Z., Barnes, S.J., Reddy, S.M., Godel, B., Fiorentini, M.L., 2013. Morphology and microstructure of chromite crystals in chromitites from the Merensky reef (Bushveld Complex, South Africa). Contrib. Mineral. Petrol. 165, 1031—1050.

Wager, L.R., Brown, G.M., 1968. Layered Igneous Rocks. Oliver and Boyd, Edinburgh, p. 588.

Walraven, F., Armstrong, R.A., Kruger, F.J., 1990. A chronostratigraphic framework for the north-central Kaapvaal craton, the Bushveld complex and the Vredefort structure. Tectonophysics 171, 23—48.

Willmore, C.C., Boudreau, A.E., Kruger, F.J., 2000. The halogen geochemistry of the Bushveld Complex Republic of South Africa: implications for chalcophile element distribution in the lower and critical zones. J. Petrol. 41, 1517—1539.

Zeh, A., Ovtcharova, M., Wilson, A.H., Schaltegger, U., 2015. The Bushveld Complex was emplaced and cooled in less than one million years — result of zirconology, and geotectonic implications. J. Earth Planet. Sci. Lett. 418, 103—114.